Supplementary Information (SI) for EES Batteries.

Supporting Information

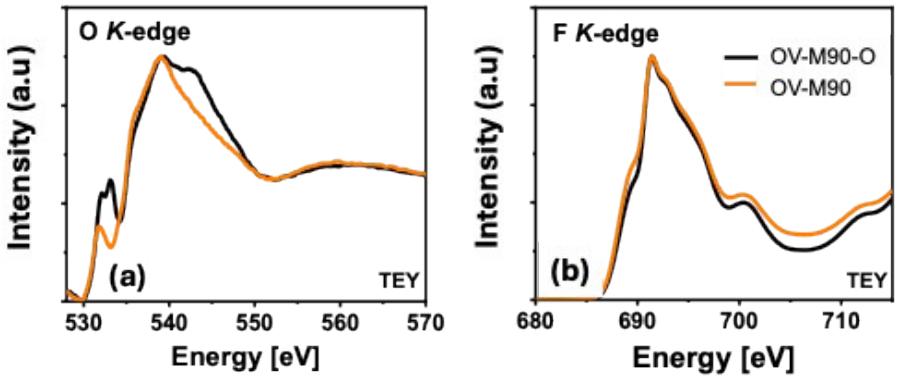

Figure S1. (a) TEY oxygen *K*-edge XAS profiles and (b)TEY fluorine *K*-edge XAS profiles of OV-M90-O and OV-M90.

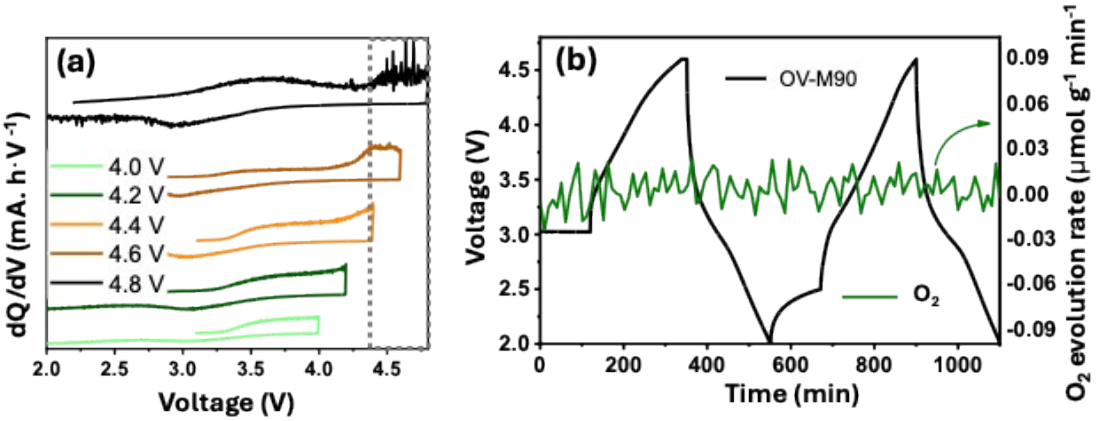

Figure S2. (a) 1st cycle dQ/dV plots of the cells cycled in various voltage windows of 2.0-4.0 V, 2.0-4.2 V, 2.0-4.4 V, 2.0-4.6 V, and 2.0-4.8 V, and (b) voltage profile and oxygen evolution during the DEMS measurement of OV-M90 in the first 2 cycles.

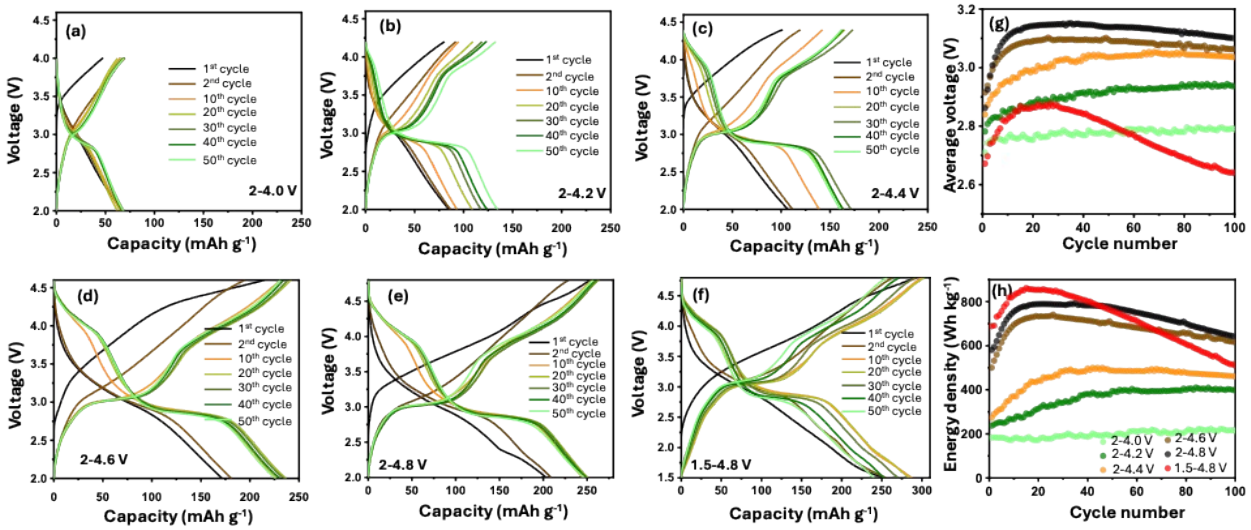

Figure S3. (a-f) Voltage profiles of OV-M90 cathode cycled at 30 mA/g in the voltage window of 2-4.0 V, 2-4.2 V, 2-4.4 V, 2-4.6 V, 2-4.8 V and 1.5-4.8 V, respectively. (g, h) Average voltage and energy density as a function of cycle number, respectively.

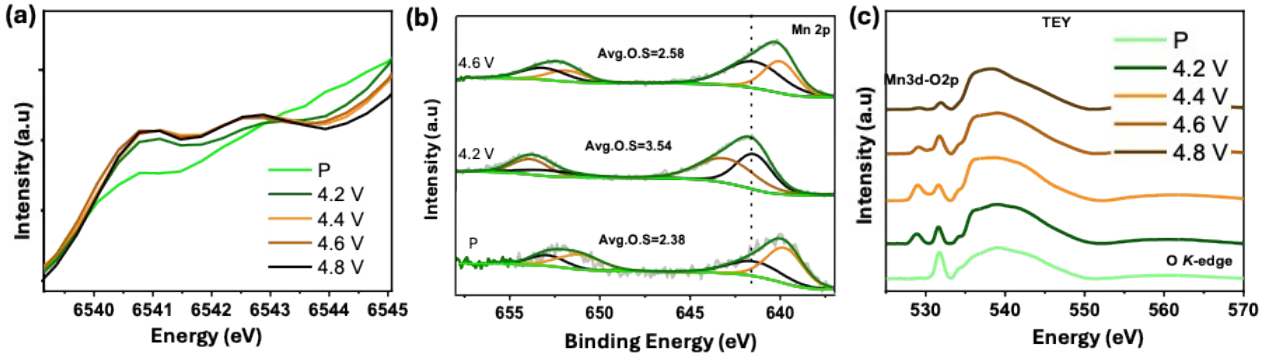

Figure S4. (a) Expanded view of the XANES pre-edge spectra, (b) Mn2*p* XPS profiles, and (c) TEY Mn *L*-edge XAS profiles of the OV-M90 cathode at the pristine (P) and various charged states in the first cycle.

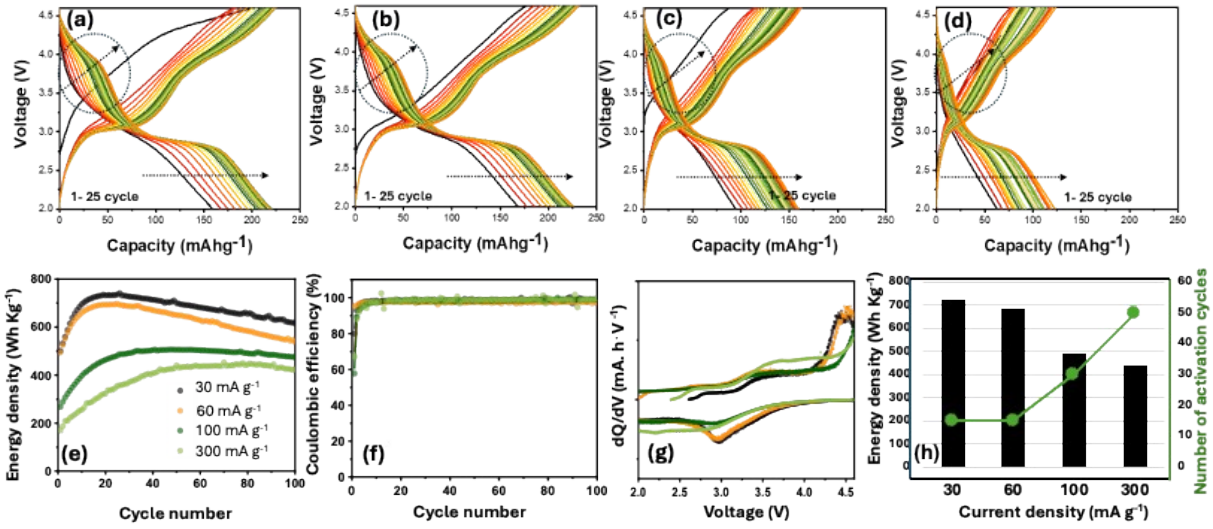

Figure S5. (a-d) Voltage profiles when cycled between 2-4.6 V at various current densities of 30, 60, 100, and 300 mA g^{-1}, respectively. (e, f) energy density and coulombic efficiency as a function of cycle number, respectively (g) the 1st cycle dQ/dV plots, and (h) comparison of maximum energy density and number of activation cycles of OV-M90 cathode when cycled at various current densities of 30, 60, 100, and 300 mA g^{-1}.

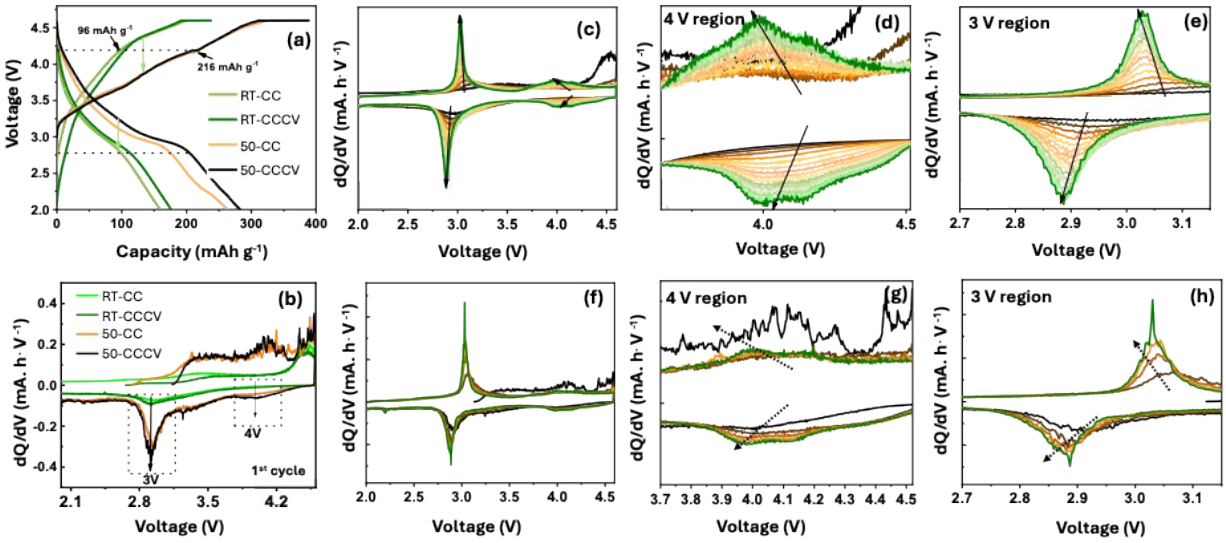

Figure S6. (a, b) Comparison of the 1st cycle voltage profiles and the corresponding dQ/dV profiles of the OV-M90 cathode cycled under four differenet activation protocols as indicated. (c-e) The evolution of the dQ/dV profile upon cycling of the OV-M90 cathode using the RT-CC protocol. (d, e) show the expanded views of the 4 V region and 3 V region, respectively. (f-h) The evolution of the dQ/dV profile upon cycling of the OV-M90 cathode using the 50-CCCV protocol. (g, h) show the expanded views of the 4 V region and 3 V region, respectively.

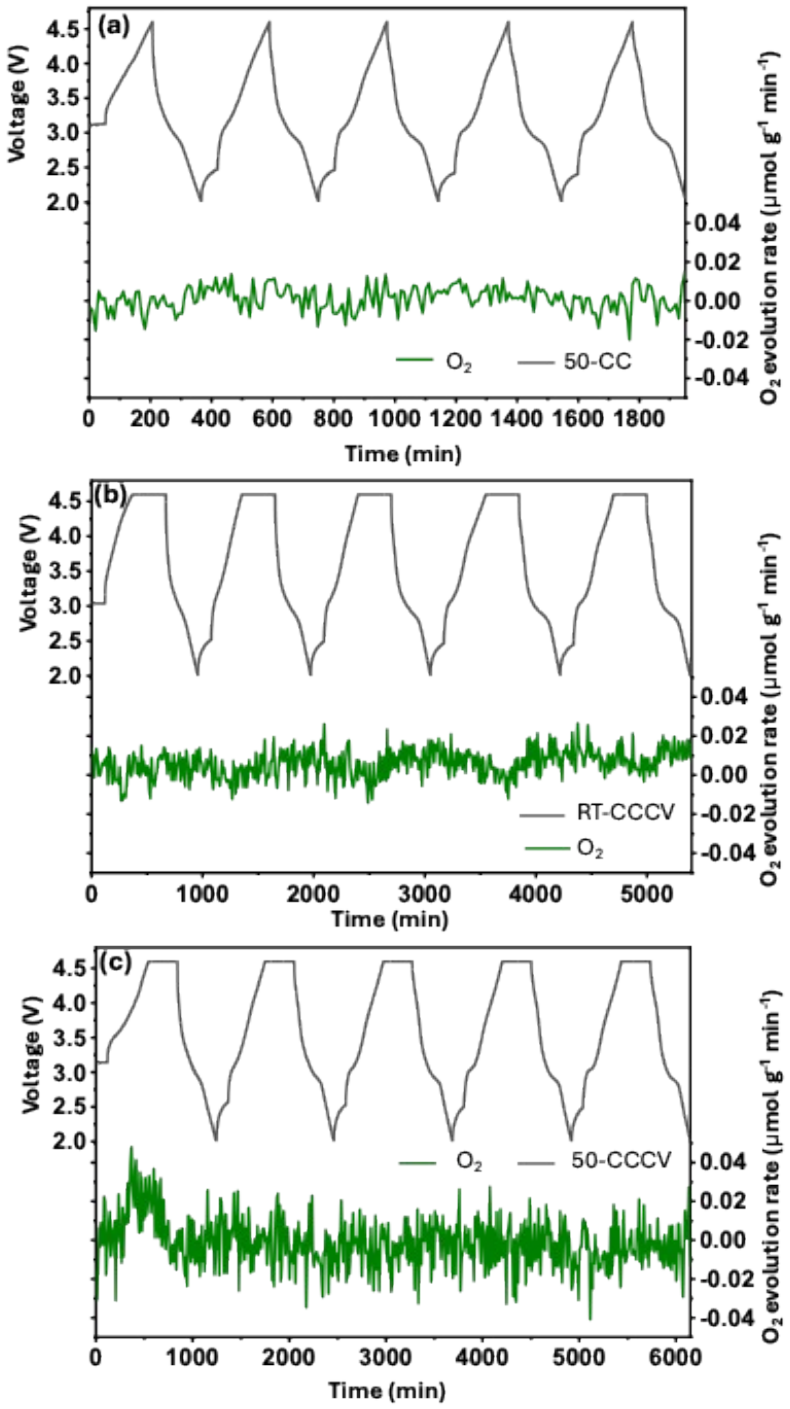

Figure S7. DEMS measurements of OV-M90 cathode during the first 5 cycles using different cycling protocols: (a) 50-CC, (b) RT-CCCV, and (c) 50-CCCV.

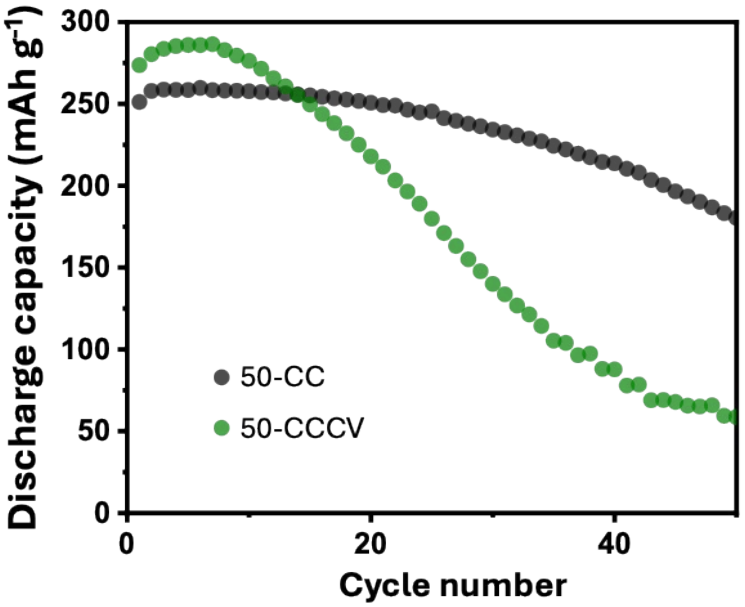

Figure S8. Cycling performance comparison of OV-M90 at 50°C using the protocols as indicated.

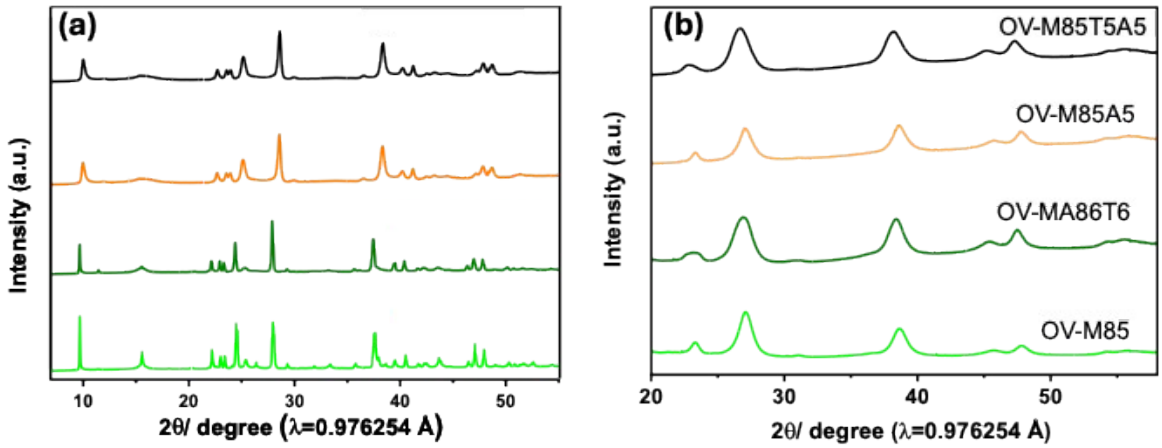

Figure S9. Synchrotron XRD of the cathode materials before (a) and after (b) ball milling, showing the transformation from an ordered orthorhombic phase to a disordered rocksalt phase upon ball milling.

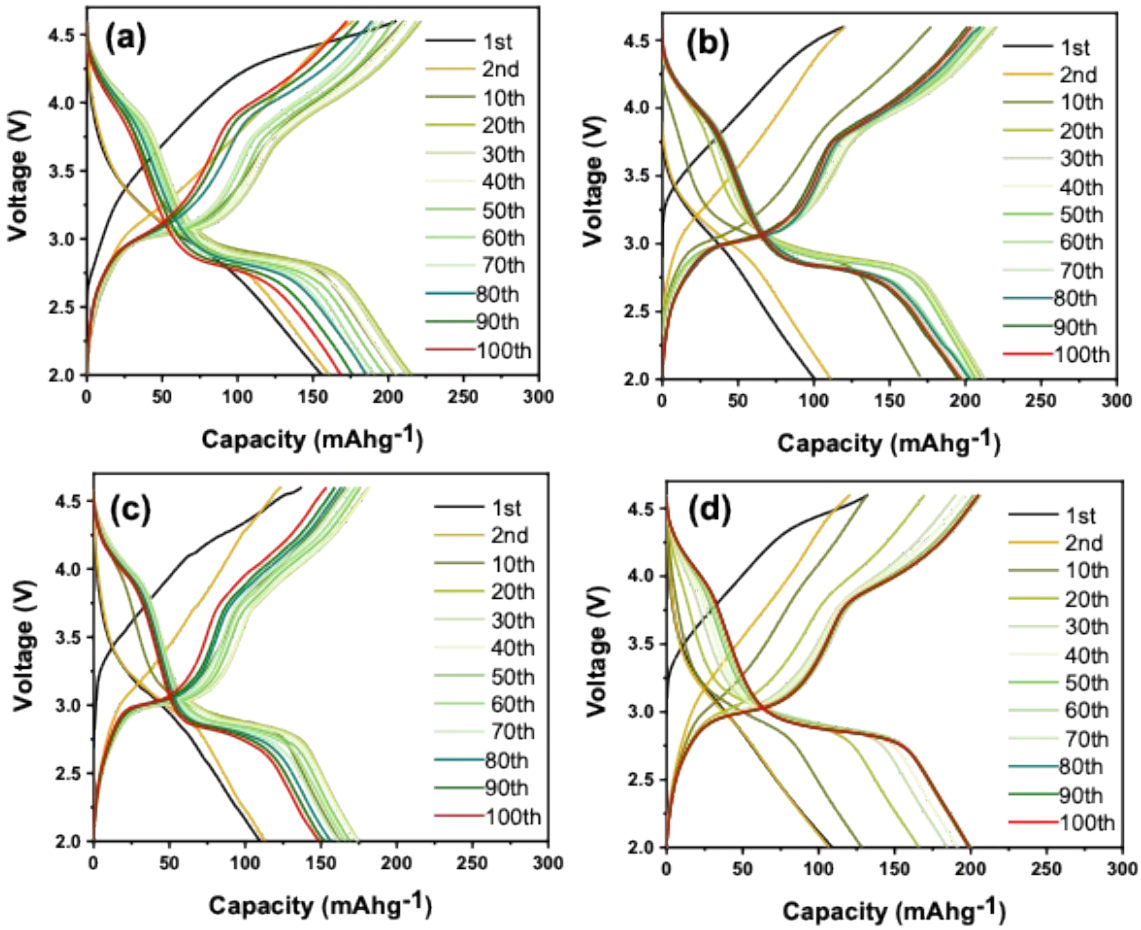

Figure S10. Voltage profiles of (a) OV-M85, (b) OV-M86T6, (c) OV-M85A5, and (d) OV-M85T5A5 cathodes during first 100 cycles. The data is shown in 10 cycle intervals.

Table S1. Comparison of ionic radius, bond strength, and the nature of the Mn-O, Al-O, and Ti-O bonds

Bond Type	Ionic radius (Å) (6-coordinated)	Bond Strength (kJ/mol)	Bond Strength (eV)	Notes
Mn^{2+}-O	0.83	~ 402	4.2	Predominantly ionic
Mn^{3+}-O	0.645	~ 443	4.6	Partially ionic, partially covalent
Mn^{4+}-O	0.53	~ 523	5.4	Predominantly covalent
Al-O	0.535	~ 512	~ 5.30	Predominantly ionic with some covalent contribution
Ti-O	0.605	~ 670	~ 6.95	Strong bond due to a mix of covalent and ionic characters

References

1. P. Atkins, J. de Paula, and J. Keeler, *Atkins' Physical Chemistry*, 11th Edition, Oxford University Press, 2017.
2. F. A. Cotton and G. Wilkinson, *Advanced Inorganic Chemistry*, 6th Edition, Wiley, 1999.
3. Shannon, R. D., "Revised effective ionic radii," *Acta Cryst. A32*, 1976.